33RD CONGRESS
OF THE INTERNATIONAL COUNCIL
OF THE AERONAUTICAL SCIENCES
STOCKHOLM, SWEDEN, 4-9 SEPTEMBER, 2022

ICAS 2022 SWEDEN

AEROSHAPE AND TRAJECTORY DESIGN OF NEXT GENERATION RE-ENTRY VEHICLES

Nicolina Montella, Andrea Aprovitola, Luigi Iuspa, and Giuseppe Pezzella

University of Campania "L.Vanvitelli",

Department of Engineering, Via Roma 29, I-81031. Aversa (CE), Italy.

Abstract

The design of reusable re-entry vehicles is unavoidably dictated by the specific strategy for thermal barrier management, depending on which type of re-entry, ballistic or lifting, the vehicle exploits during decent. Although resembling some features typical of the Space Shuttle (e.g., blunted nose, curved leading-edge, etc.), the general design of next generation lifting vehicles like Dream Chaser and X37-B, reflects the large difference envisaged for the re-entry phase. Specifically, reduced dimensions and seamless wing bodies body, allows a more gradual and sustainable conversion of potential energy in kinetic and thermal energy. Therefore, affordable re-entry options compatible with reusable spacecrafts are a key-technology for a future vehicle concept. The above considerations underline the important mutual influence between re-entry strategies and vehicle aerodynamic performances as early as preliminary design phase.
In this context, the present paper aims at conjugating the aeroshape design procedure for a reusable re-entry vehicle with an optimal flight strategy aimed to keep constant the heat flux inside a predicted threshold. Starting from a simplified radiative equilibrium hypothesis, a multidisciplinary optimization is used to determine the optimal shape of the vehicle. The adopted modelling procedure allows the procedural generation of blended lifting bodies with high surface-to-mass ratio to maximize aerodynamic performances in a multi-regime re-entry. To prevent a dangerous overheating of the vehicle, an additional optimization procedure determines the best re-entry flight strategy from low-Earth orbit. An optimization problem is formulated to determine the prescribed optimal guidance law, which parametrically modulates the angle of attack with respect to the Mach number. The Simulation formalizing an objective function accounting for the fitting between trajectory curve and thermal boundary is also performed. The best re-entry condition is discussed with respect to thermal feasibility of the preliminary aeroshape design.

Keywords: Spacecraft, LEO re-entry, heat flux control, multi-disciplinary design optimization, guidance law.

1. Introduction

In the last decades, researchers and industries retrieved the Space Shuttle design and adapted it to current mission requirements.

The Shuttle was designed for large payload transport, *e.g.*, satellites and instrumentations; consequently, a very large 18 m long and 4.6 m wide payload bay was provided. Current Crew Return Vehicles (CRV) are instead most intended as a way to transport and support crew-members from the International Space Station (ISS) to the Earth.

Consequently, present re-entry vehicles like the Dream Chaser spacecraft, developed by NASA and SNC company, have different aerodynamics and lower dimensions than Space Shuttle (9 m long with a wingspan of 7 m). However, the Dream Chaser still maintains several features in common with its precursor, such as a delta-shaped planform lifting-body, also replicating the same thermal barrier management and re-entry strategy of the Shuttle. In addition, similarly to early lifting bodies developed in 1970's, the Dream Chaser is designed to perform a low-g re-entry (max 1.5g), a horizontal landing on runway, and it is re-usable and maneuverable at low-speed.

In general, the main issue that deals with this type of vehicle is the high aerothermal load. In particular, the complexity and fragility of the Space Shuttle Thermal Protection System (TPS) makes re-entry

less safe for the crew (as evidenced by the second unfortunate Shuttle failure). Moreover, the non-complete re-usability of TPS resulted in huge costs for its refurbishments, with a very high experimental efforts spent to develop efficient insulation tiles during Shuttle ground test campaigns.

The reason why the TPS was replaced during every re-entry can be explained by considering that the re-entry procedure performed by the Space Shuttle, relied on previous matured experience with re-entry capsules. These capsules, *e.g.*, Mercury, Gemini, and Apollo, performed a ballistic re-entry with blunt shapes and high Angle of Attack (AoA), that means flying with a large drag coefficient and, consequently, a high amount of vehicle total energy that must be dissipated in a very short time interval [1].

Aim of the present research work is to analyze different re-entry strategies of that of the Space Shuttle, allowing a more gradual conversion of vehicle energy able to keep the convective heat flux within a more favorable range. In this way, a reusable spacecraft, which is the key-technology for a future vehicle concept [2], is possible.

For that purpose, starting from a simplified radiative equilibrium hypothesis, a multi-disciplinary optimization is used to determine the optimal shape of the vehicle [3]. Therefore, a spacecraft configuration which performs a suitable re-entry strategy was preliminarily developed. In particular, the authors have developed a re-usable Blended Wing Body (BWB) vehicle with a rather high surface-to-mass ratio $\mathrm{S_r/m}$ (Figure 1) that can access to space in Low Earth Orbit (LEO) and return on a conventional runway with horizontal landing [4], [5].

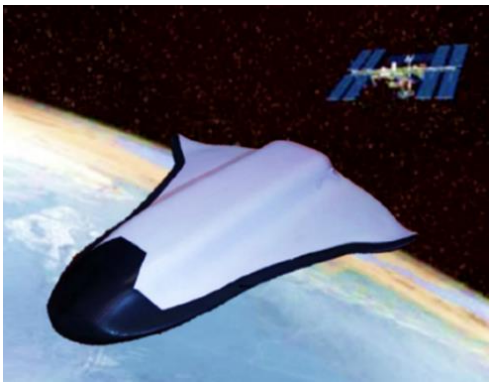

Figure 1 - Pictorial representation of the Spacecraft in orbit.

This configuration is the result of a multi-objective optimization procedure. The spacecraft shape was described by a parametric model, and the optimization procedure changes a set of non-dimensional parameters which modify the shape morphology globally. Aim of this optimization procedure is to minimize the vehicle mass and maximize its cross-range; the proposed configuration, chosen among the equally optimal solutions collected by the Pareto front, can cover up about 10 km of down-range and 1 km of cross range. In addition, in Ref. [6] a more useful TPS modelling procedure was implemented to perform a shallower re-entry. Then, CFD simulations have been performed to validate vehicle aerodynamics at hypersonic and supersonic speeds, as described in Ref. [7]. As concern vehicle low-speed aerodynamics (i.e., $M_\infty = 0.3$), two functionally independent body flaps are integrated in the vehicle design to control both longitudinal and/or lateral-directional stability, as described in Ref. [8]. In this way, preliminary information about runway landing capability is provided.

Once the vehicle configuration is outlined, it can be used to experiment a more effective re-entry procedure. To get longer the re-entry time interval, a very extended gliding trajectory (of magnitude hour order) is performed, differently than the Space Shuttle that lasts only about 30 minutes. As the aero heating depends on the duration of conversion of vehicle initial kinetic energy per unit mass (*e.g.*, about $30\ \mathrm{MJ/kg}$), having a longer re-entry time helps to keep a lower convective heat flux level. In addition, if this level is kept constant for enough time, a re-usable TPS that takes advantage of radiative cooling could be used, without the necessity to replace it at every mission.

The above re-entry strategy can be performed flying with small S_r/m ratio configurations and at small

flight path angle ($\gamma \ll 1$). These characteristics not only allow to reach lower surface temperatures because the glider will fly at high altitudes with small AoA for a longer time (high-lift configurations dictate lower angles of attack and *vice versa*, as described in Ref. [9]), but also allow a landing on conventional runways, within a wide footprint. This certainly allows to improve rescue capabilities of the CRV but, on the other hand, some operational difficulties could still exist flying for a longer period, (e.g., tracking and thermal protection of crew and equipment).

The purpose of keeping the convective heat flux level at a definite threshold for a certain time can be followed through a prescribed Guidance Law (GL) which modulates the AoA in function of the descent Mach number. A parametric model of GL is implemented, and the performance is measured through the heat flux time-history, where a near-constant heat flux target represents the goal. Different heat flux levels will be analyzed to ensure a certain safety margin. An in-house procedure that allows to design the prescribed GL and integrates the related trajectory is implemented through the Ansys Parametric Design Language (APDL) Environment. The GL has been modelled using parametrization with parametric cubic splines. Then, different single-objective optimization procedures, driven by a genetic algorithm, are performed to discover not only the GL that best meets our requirements, but also the initial best flight path angle γ_0 and bank angle μ_{a_0} chosen from two respective intervals.

2. Research background

The Space Shuttle returns from LEO with a lifting re-entry maneuver. Unlike capsules, Winged Bodies (WB) are designed to glide into the atmosphere and land on a conventional runway. For this reason, the Shuttle re-enters with a small flight path angle ($\gamma = -1.2°$) at a speed equal to about $V_e = 7.6\ km/s$.

Flight path angle value is very important to obtain a re-entry as shallow as possible. In the Literature, several heat flux tracking procedures on which a re-entry optimization is based, can been found. However, they basically differ on the value of the re-entry fly path angle which sets the mission requirements (*i.e.*, civilian vs military mission). In Zhou et al. [10] two approaches are considered to find the GL that best sets the mission requirements: respectively, an off-line trajectory design approach, and an on-line trajectory design one. The first methodology prescribes the AoA profile and uses feedback to control deviation in the lateral plane of trajectory in order to keep the vehicle inside the re-entry corridor [11]. However, in this approach the re-entry corridor and the bank modulation have to been determined, and this fact complicates the problem. The second approach is characterized by a drastic increase of computational cost due to the reiterate online optimization of the trajectory [12].

Another heat tracking system, designed for a stagnation point heat flux $\dot{q}_c = 740\ kW/m^2$ for a flight path angle $\gamma = -0.5°$, was considered by Dirkx and Mooij [13] to test new insulating materials. This tracking system correlates the heat flux error with the drag modulation through a proportional integral regulator.

In Ref. [14], a max value of $500\ kW/m^2$ heat flux peak at stagnation point was considered as constrain for a global optimization of the re-entry trajectory applied to a spacecraft with $L/D = 0.7$ and $\gamma = -1.43°$. The above optimization was performed through a modulation of AoA obtained with a second order law.

As described in the previous sections, the re-entry phase for Hypersonic Gliding Vehicles (HGV) is very critical because of thermal heating problems. Therefore, Chawla et al. [15] designed a trajectory optimization of an HGV accounting for heat rate constraint and maximum dynamic pressure with the modulation of the $\mathrm{L/D}$ ratio and the heat flux rate with the AoA, during the glide phase in sub-orbital segment.

In addition, Zhao et al. [16] analyzed the orbital re-entry trajectory of a Common Aerial Vehicle (CAV) using convex programming. In this research work, a flight path angle $\gamma = -1.5°$ and a heat constraint $\dot{q}_0 = 4000\ kW/m^2$ were assumed, and a bank angle and lift coefficient optimization were performed, considering heat flux, dynamic pressure, and path constraints in terms of no-fly zones.

3. Research framework

The current approach, unlike those ones described in literature, allows to explore re-entry strategies without using an explicit control feedback. In particular, to perform a shallower re-entry which allows a longer re-entry time interval, and consequently a constant value of a convective heat flux, a heat flux targeting procedure is developed. This procedure provides a parametric formulation of a GL using natural splines through eight control points that parametrically vary their coordinates expressed in terms of AoA and Mach number.

In addition, differently than what was done in the work of (Aprovitola, Ref. [9]), the flight path angle and the bank angle at the beginning of re-entry phase ($V(t_0) = 7830\ m/s$) are not fixed, but can be chosen by the optimization procedure within suitable ranges that possibly can take into account the necessity to have a shallower re-entry.

The optimization problem was performed through a genetic algorithm; control points coordinates of the GL are defined as design variables, together with the flight path angle and bank angle at the beginning of the re-entry phase. Given the re-entry corridor in Figure *6*, the objective function is the area between the trajectory and the thermal constraint curve in the higher phase of the re-entry. As shown in [9],the trajectory has to lie on the thermal constraint curve to guarantee a constant heat flux at stagnation point. In this work, different heat flux level will be considerate. The constraint is represented by the dynamic pressure boundary which mustn't be overcome by the trajectory. The fully reusability of the vehicle can be promoted by the robustness of the evolutionary algorithm.

3.1 Vehicle configuration

In Figure 2, the optimized shape of the re-entry vehicle considered for the application of the procedure previously described is shown. The vehicle has the following dimensions: $l_t = 9.25\ m$ (total length); $h = 1.5\ m$ (total height); $h_{ws} = 4.3\ m$ (half wingspan); $r_n = 0.469\ m$ (nose radius); $\theta = 40°$ (bent angle).

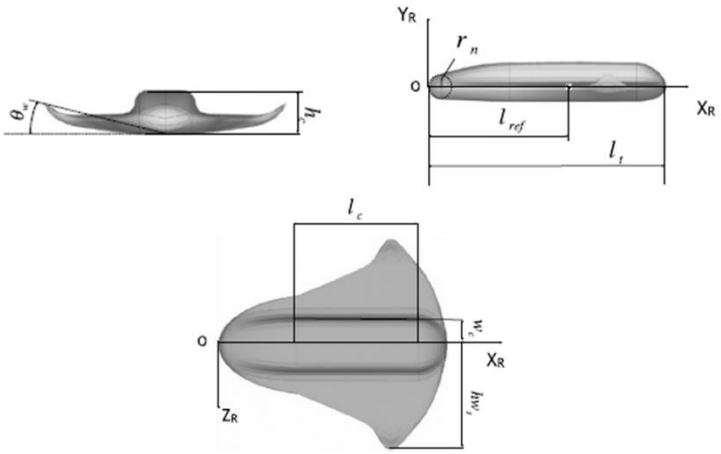

Figure 2 – Optimized shape for the re-entry vehicle conceptual design.

This aeroshape was deliberated through a multi-disciplinary optimization procedure that both minimized the overall weight and maximized the cross-range, also allowing the vehicle to easily approach the landing on a conventional runway. In addition, the concept satisfies a set of requirements essential for a LEO re-entry mission, as described in Ref. [4], [5] and [7]. In particular, this configuration can support the thermal dissipation features through a rather blunt flat-bottomed aeroshape, and it is able to improve low aerodynamics through a high swept delta planform, by means of vortex-lift contribution [17]. The vehicle structure insulation is assured by a passive TPS, made of blankets and ceramic tiles. In particular, wing leading-edge, nose, tip fins and aerodynamic control surfaces are coated with a high-temperature, carbon silicon-carbide hot-structure with a surface coating (Figure 1, [18]). Further details about this vehicle concept can be found in Ref. [19].

3.2 Vehicle aerodynamics

The analysis of vehicle aerodynamics is mandatory to evaluate a spacecraft re-entry trajectory,

especially in the hypersonic phase, where the thermal barrier constraint is important. High-speed vehicle aerodynamics are discussed in detail in Ref. [7].

An APDL procedure has been developed to generate a multi-regime aerodynamic database, which provides lift and drag coefficient for any combinations (α, M_∞) during re-entry through a bi-linear interpolation/extrapolation by the trajectory integration code.

4. Heat flux targeting procedure

A flowchart of heat flux targeting procedure is shown in Figure 3.

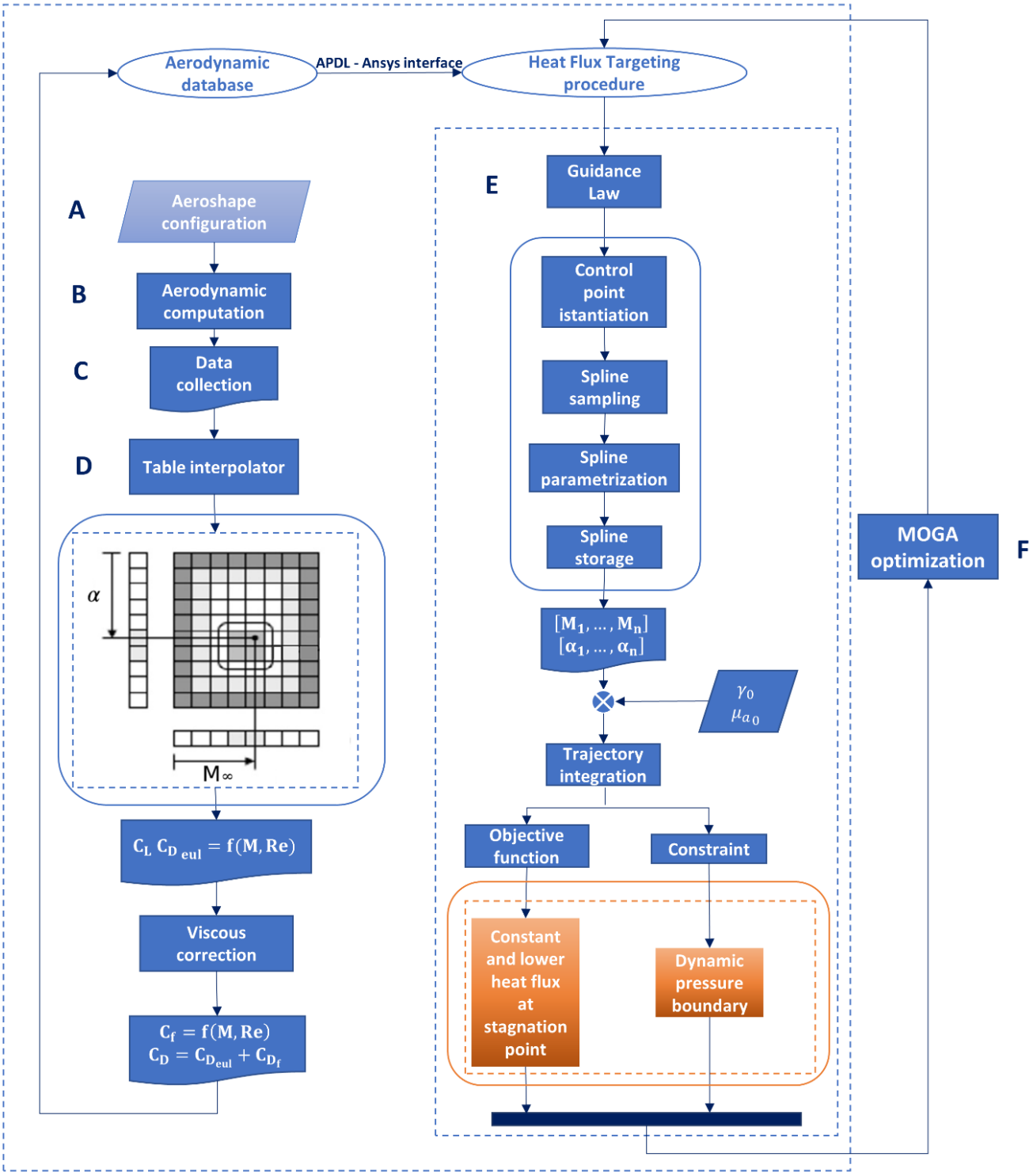

Figure 3 - Heat flux targeting procedure flowchart.

The entire procedure has been implemented in the APDL-ANSYS parametric environment.

Starting from the current configuration extracted from the search space (block A) modelled as a panel surface mesh (Refs. [4] [5]), the procedure provides to create a proper aerodynamic database collecting lift and drag coefficients (C_L and C_D) by enveloping two arrays, respectively $M_\infty = [2, 4, 6, 8, 10, 15, 20, 25]$, and $\alpha[0°, 5°, 10°, 15°, 20°, 25°, 30°, 35°, 40°, 45°]$.

In particular, a low fidelity engineering approach is used to perform the aerodynamic computation; specifically, Surface Inclination Method (SIM) is used for both supersonic and hypersonic aerodynamic computation, while a panel method based on the potential flow theory is employed for subsonic regime (block B).

Then, aerodynamic data are collected in a two-dimensional table data structure (block C) which computes on-demand aerodynamic coefficients required by the trajectory module using a bi-linear, quadratic interpolation or extrapolation where needed (block D).

Viscous contribution is added only to the drag force through the term C_{Df} which is relied on the total friction coefficient C_f:

$$C_{Df} = \frac{S_{wet}}{S_{ref}} C_f \tag{1}$$

where S_{wet} is the spacecraft wetted surface.

Coefficient C_f is provided by the Schlichting's relationship [20] for compressible and turbulent boundary layer conditions, evaluated after the bi-linear quadratic interpolation, and accounting for the similarity parameters (i.e., Mach and Reynolds) effects:

$$C_f = \frac{0.42}{[log_{10}(Re_{l_{ref}})]^{2.55}\left(1+0.25M_\infty^2\right)^{0.31}} \tag{2}$$

Once defined the input environment, a parametric expression for the GL (*i.e.*, AoA versus the Mach number) is derived using natural splines in order to obtain a more flexible trend (block E).

In particular, eight control points are introduced to model the GL profile; these control points vary their position on the Mach-AoA plane trough normalized parameters.

Subsequently, the GL instance is then transferred to a trajectory RK4 integrator, which uses the guidance law sampling and the aerodynamic database to return the trajectory related to the vehicle and guidance law instances.

The results are then given to the optimization algorithm which provides for choosing the set of variables (GL non-dimensional parameters, initial flight path angle γ_0 and bank angle μ_{a_0}) that best satisfied a proper objective function, also assuming a set of constraint functions.

Block F of the flowchart represents the optimization algorithm that chooses the best set of variables. For this analysis, a Floating-point Genetic Algorithm (FpGA) has been used.

4.1 Trajectory integration

In the present work, the spacecraft has been approximated as a two degrees of freedom point mass plus a futher modulation of the AoA provided by the selected guidance law, over a non-rotating spherical Earth.

The equations of the motion of the spacecraft are projected along the flight path tangential/normal directions (Figure 4):

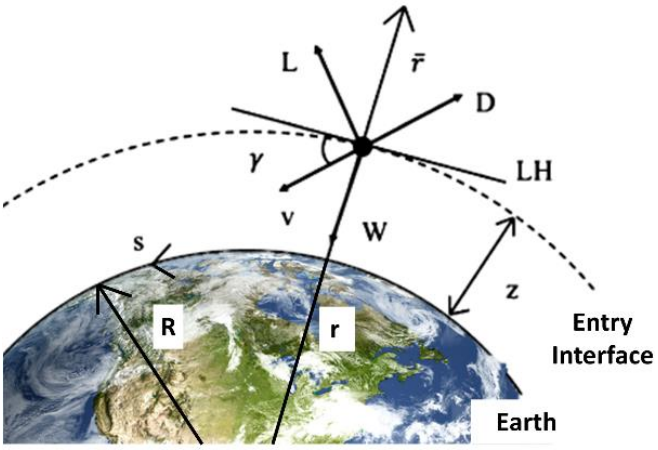

Figure 4 - Atmospheric re-entry layout.

$$\frac{dv}{dt} = -\frac{D}{m} - g\sin\gamma \tag{3}$$

$$v\frac{d\gamma}{dt} = \frac{L}{m}\cos\mu_a - \left(g - \frac{v^2}{r}\right)\cos\gamma \tag{4}$$

altitude (z), and down-range (s) are expressed as follows:

$$\frac{dz}{dt} = v\sin\gamma \tag{5}$$

$$\frac{ds}{dt} = \frac{R}{r}v\cos\gamma \tag{6}$$

where:

$$g = g_0\left(\frac{R}{r}\right)^2 \tag{7}$$

and:

$$\begin{cases} L = \frac{1}{2}\rho v^2 c_L S_{ref} \\ D = \frac{1}{2}\rho v^2 c_D S_{ref} \end{cases} \tag{8}$$

Banking modulation is not considered in the present model for the sake of simplicity (*i.e.*, planar re-entry motion). Therefore, aerodynamic characteristics C_L and C_D depend on the AoA, α, and the flight Mach number, M_∞, and Reynolds number, Re_∞.
For the integration of these equations, initial conditions are given assuming $h(t_0) = 120\,km$ and speed $V(t_0) = 7830\,m/s$.
Starting values for longitude, latitude, and flight azimuth are set to zero.
The dependence between the flight duration Δt and the aerodynamic efficiency was analyzed in Ref. [9]:

$$\Delta t \cong \frac{\overline{C_L}}{\overline{C_D}} \overline{f_t}(\rho, v) \tag{9}$$

where $\overline{C_L}/\overline{C_D}$ is the average aerodynamic efficiency along the trajectory and $\overline{f_t}(\rho, v)$ is the average of $\left(g - \frac{v^2}{r}\right)\frac{v}{\sqrt{\rho}}$ along the trajectory.

From Figure 4, it is simple to recognize the dependence between the aerodynamic efficiency and flight path angle. Therefore, considering Eq. (8), the dependence between flight path angle and re-entry time is easily recognizable.

The total flight time is also influenced by the bank angle because it modulates the lift; consequently, the bank angle has effects on the aerodynamic efficiency.

The effective lift, L_{eff}, and the side lift L_{side} are defined as (Figure 5):

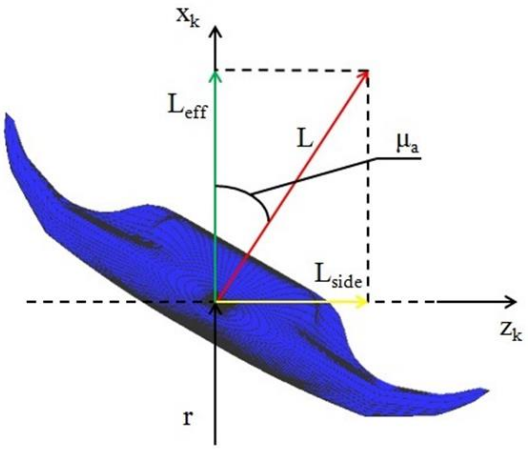

Figure 5 - Schematic definition of the bank angle.

$$L_{eff} = L\cos\mu_a$$
$$L_{side} = L\sin\mu_a \tag{10}$$

From Eq. (10), being L_{eff} less than the total lift L, the effective aerodynamic efficiency L_{eff}/D is lower than L/D, therefore an increasing of μ_a causes a reduction of the real efficiency and, through Eq. (9), the re-entry time.

The bank angle also affects the down range Δx_p (spacecraft ground track in the spacecraft longitudinal direction), and the cross range Δy_p (spacecraft ground track in the spacecraft lateral direction), by the following set of equations (Ref. [21]):

$$\Delta x_p \sim \frac{L}{D}\cos\mu_a$$
$$\Delta y_p \sim \frac{L}{D}\sin\mu_a \tag{11}$$

It is possible to observe that a positive cross range is associated to an increase of the bank angle μ_a.

In order to withstand the mechanical and thermal loads during the descent, the spacecraft should operate within a proper re-entry corridor bounded by: *i*) the equilibrium glide limit at high altitudes; *ii*) the aeroheating boundary and the normal load factor constraint at lower altitudes, as shown in Figure 6:

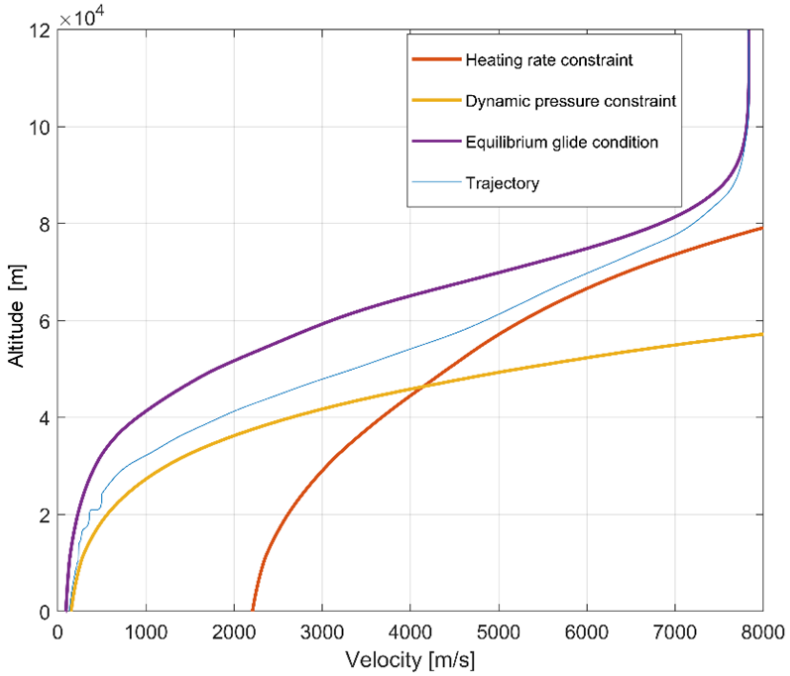

Figure 6 - The re-entry corridor and an allowable trajectory.

The aeroheating limit identifies the couple (ρ_∞, v_∞) related to maximum stagnation point temperatures T_{wr0}, that depends, at a given altitude, on the geometrical radius of curvature of the vehicle leading-edge and the Thermal Protection Material (TPM) of the heatshield.

For this analysis, T_{wr0} is assumed equal to 1792 K. The convective heat flux can be described by the Zoby's relationship:

$$\dot{q_0} = K_Z \sqrt{\frac{p_s}{R_N}} (H_0 - h_w) \qquad \left(\frac{W}{m^2}\right) \tag{12}$$

where $K_Z = 3.88\, x\, 10^{-4}$ and ρ_s is the stagnation pressure. R_N is the vehicle's curvature radius, that for the vehicle's configuration chosen is equal to 0.469 m. The equilibrium glide curve ($v^2 = cost$) (*i.e.*, the curve which governs the horizontal steady flight at the maximum C_L, $C_{L_{max}}$, assumed equal to 0.75) moves to higher altitudes as $C_{L_{max}}$ and large S_r/m ratio.
It represents the corridor roof, while the pressure limit and the normal load factor limit represent the corridor floor. Higher values of S_r/m and of T_{wr0} widen the re-entry corridor. Therefore, the flight envelope defines the limits of the allowable re-entry trajectories: couples of values (ρ_∞, v_∞) above the equilibrium glide curve mean that the vehicle cannot develop enough lift to keep flying, while couples under the aerothermal curve and the normal load factor curve mean that the vehicle cannot withstand thermal loads and mechanical loads respectively.

4.2 Guidance law

In Block E in Figure 3 the parametric expression of GL is formalized in term of the AoA expressed as function of Mach number using natural cubic splines. In Ref. [9], the number of control points is analyzed to choose which one gives the best results. Specifically, six control points in total were proposed for the interpolation of the GL: four parametric points which vary their coordinates (with a total of eight parameters), and two (fixed) boundary points corresponding to initial and final flight: $P_1(0.3, 10°)$ and $P_6(25, 45°)$ respectively. Parametric control points coordinates are defined as follows:

$$\begin{aligned} \alpha_{i+1} &= (\alpha_{i+2} - \alpha_1) \cdot Y_i + \alpha_1 \qquad (i = 4, \dots, 1) \\ M_{j+1} &= (M_{j+2} - M_1) \cdot X_j + M_1 \qquad (j = 4, \dots, 1) \end{aligned} \tag{13}$$

The re-entry trajectory path, and consequently the heat flux, can be obtained by varying Y_i and X_j within normalized ranges chosen to return reasonable functional instances:

$$\begin{gathered} Y_1 \in [0.1, 1] \\ Y_2 \in [0.2, 1] \\ Y_3 \in [0.5, 1] \\ Y_4 \in [0.6, 1] \\ X_1 \in [0.1, 0.9] \\ X_2 \in [0.4, 0.9] \\ X_3 \in [0.5, 0.9] \\ X_4 \in [0.5, 0.9] \end{gathered} \tag{14}$$

An example of typical GL formulated trough a spline passing through six control points as previously described, is shown in Figure 7.

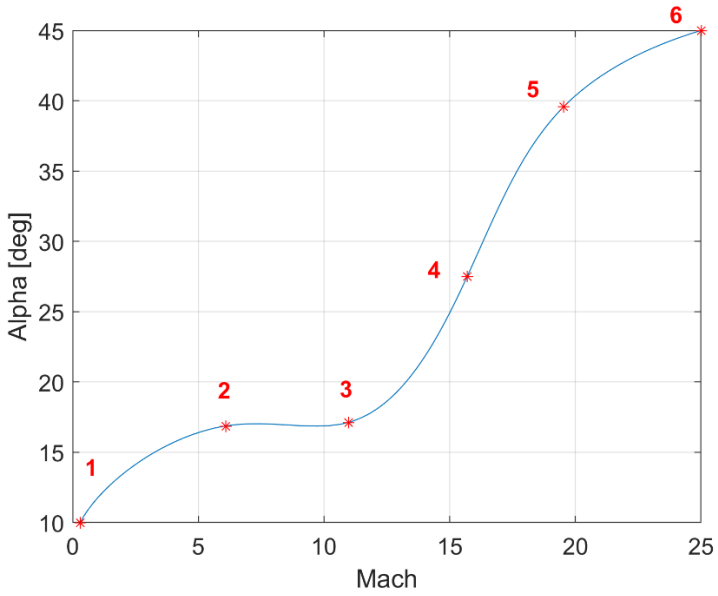

Figure 7 – Example of GL.

5. Optimization procedure

In Ref. [9], the searched GL had to guarantee a target heat flux value at stagnation point (nose radius equal to $R_n = 0.469\ m$) of $600\ \mathrm{kW/m^2}$ for the widest speed range compatible with the feasible re-entry corridor. This convective heat flux limit corresponds to a local radiative cooling temperature of about $1900\ \mathrm{K}$, for a surface emissivity of 0.8. The operating temperature range of Reinforced Carbon-Carbon (RCC), (the material typically used for the fuselage nose heat shield), is from $116.50\ \mathrm{K}$ to about $1922.05\ \mathrm{K}$ [22]. Therefore, the temperature corresponding to the target heat flux chosen for this analysis is compliant with the RCC temperature limit, but is almost at the upper limit. This means that the TPS must be perfectly compliant to prevent itself to reach temperatures greater than the upper limit. The difficulty in finding a material with a very low emissivity leads to a certain safety margin being considered on the target heat flux. The reduction of the target heat flux is precisely the rationale followed in the present work, to ensure a suitable margin of safety. The optimization problem is formulated with reference to the aeroshape described in Figure *2*. Initial entry conditions are given assuming: $V_e = 7830\ m/s$, while γ_0 and μ_{a_0} are chosen by the optimization algorithm within respectively [-0.2°, 0.2°] and [-10°, 10°]. As previously described in paragraph [4.1], the chosen flight path angle variability range provides a shallower re-entry which ensures longer re-entry flight times. In addition, the initial bank angle is assumed as a design variable but, because of no banking modulation is assigned, a restricted range is chosen. The re-entry corridor allowed for this scenario is bounded by the following operational constraints: dynamic pressure boundary $Q_{max} = 14\ kPa$; landing speed $V_L = 110\ m/s$; heat flux boundary $q_{max} = 600\ kW/m^2$. In addition to the target heat flux analysed in Ref. [9] (the floor of the corridor re-entry), four different heat flux boundary levels $\dot{q}_{0_t}$

have been considered: $500\,\mathrm{kW/m^2}$, $525\,\mathrm{kW/m^2}$, $550\,\mathrm{kW/m^2}$ and $575\,\mathrm{kW/m^2}$, to obtain safer solutions. In other words, keeping the re-entry corridor unchanged, the trajectory is enforced to follow reduced heat flow levels having, at the same time, a substantial constant trend that allows an advantage about radiative cooling (
Figure *8*).

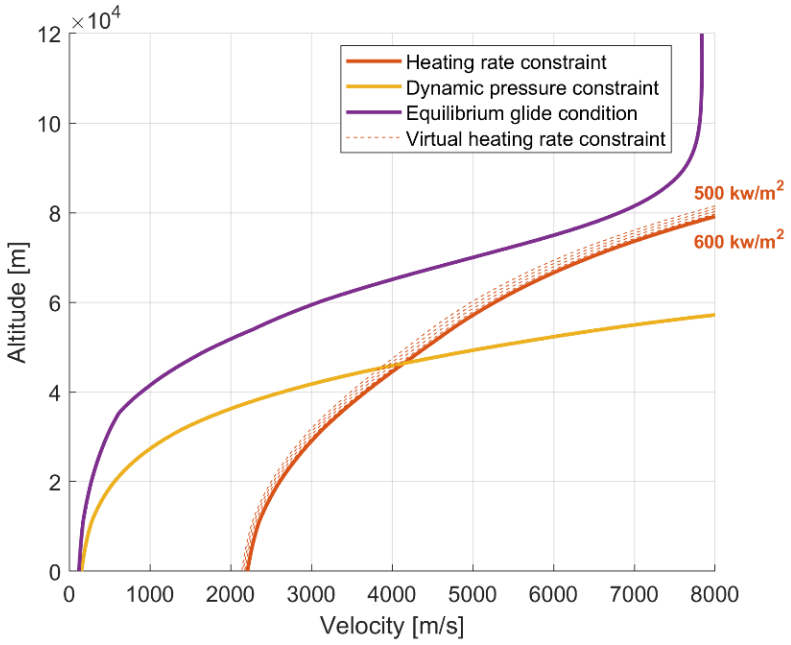

Figure 8 - Re-entry corridor with different level of thermal constraint.

5.1 Objective function and constraints

To reach a constant heat flux at the vehicle stagnation point, the vehicle trajectory should lie on the assigned heating constraint curve. Starting from the max altitude experienced at the beginning of the re-entry, the trajectory can follow the heating constraint curve up the point C_r, in which the assigned heating constraint curve intersects the maximum allowed dynamic pressure.
Starting from C_r, the trajectory must respect also such constraint. Once C_r is determined, the subtended area between trajectory and the current heating constraint curve is calculated in the Mach range ($M_\infty = 25$, M_{Cr}) (Figure 9).

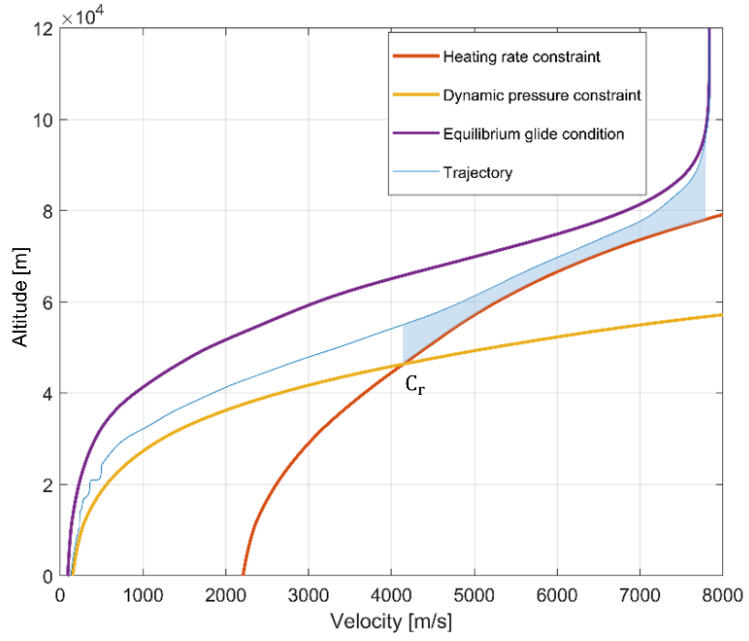

Figure 9 - Objective function definition.

This enclosed area represents the objective function to be minimized. Formally this function is expressed as follows:

$$\Delta A(\boldsymbol{x}) = \int_{M_{C_r}}^{M_\infty} (h^t - h^q) dM_\infty \approx \sum_{i=1}^{n-1} \left(A_i^t - A_i^q\right) \tag{15}$$

having denoted with $h^t = h^t(M_\infty)$ and $h^q = h^q(M_\infty)$ the trajectory and the assigned thermal boundary curve as functions of Mach number, while $\boldsymbol{x}$ is the current design vector and A_i^t and A_i^q are the areas below the curves numerically evaluated, providing a uniform sampling of h^t and h^q with n points. In this paper, h^q is referred not only to the real heat flow constraint curve ($q_{max} = 600\ kW/m^2$), but also to the virtual ones, i.e., heat flow constraint curves corresponding to a target heat flux (at stagnation point) respectively of $500\ \mathrm{kW/m^2}$, $525\ \mathrm{kW/m^2}$, $550\ \mathrm{kW/m^2}$ and $575\ \mathrm{kW/m^2}$.
To account for negative values of $\Delta A(\boldsymbol{x})$, Eq. (15) has been rewritten to implicitly integrate a penalty function that considers negative contributions to sum:

$$\Delta A(\boldsymbol{x}) \approx \begin{cases} \sum_{i=1}^{n-1} \left(A_i^t - A_i^q\right) & if \quad A_i^t > A_i^q \\ \sum_{\substack{i=1 \\ i \neq (k_1 \dots k_n)}}^{n-1} \left(A_i^t - A_i^q\right) + \sum_{k=k_1}^{k_n} p \cdot \left|A_k^t - A_k^q\right| & if \quad A_k^t < A_k^q \end{cases} \tag{16}$$

Where p is the penalty factor. If trajectory perfectly matches the heat flux boundary, the objective function returns zero, while if $\left(A_i^t - A_i^q\right) < 0$, its modulus is multiplied with coefficient p, and cumulated according to Eq. (16). The trajectory must also satisfy the dynamic pressure constraint to obtain a globally feasible solution. For $M_\infty > M_{C_r}$ the dynamic pressure constraint is always satisfied because of the formulation of the objective function; for Mach numbers $M_\infty < M_{C_r}$ an explicit constraint is required to take into account possible violations of the dynamic pressure limit:

$$g(\boldsymbol{x}) = \begin{cases} 0 & if \quad h_i^t - h_i^d \geq 0 \\ \sum_{i=k_1}^{k_q} \left|h_i^t - h_i^d\right| & (k_1, \dots, k_q) \quad h_i^t - h_i^d < 0 \end{cases} \tag{17}$$

When $h_i^t - h_i^d$ represents the altitude difference between current trajectory and dynamic pressure limit h_d computed at the same *i*-th point along the descent. If at generic point k_i the difference is negative, this means that at that sampling point the trajectory overcomes the dynamic pressure boundary, and consequently the difference $\left|h_i^t - h_i^d\right|$ is accumulated into the function $g(\boldsymbol{x})$ that becomes bigger and bigger as violations on dynamic pressure increase. Therefore, a fully feasible trajectory with respect to the dynamic pressure, implies $g(\boldsymbol{x}) = 0$.
The optimization problem is then formalized as follows:

$$\begin{matrix} \min \Delta A(\boldsymbol{x}) \\ \underline{x_i} \leq x_i \leq \overline{x_i} \qquad i = 1, 2, \dots, I \\ g(\boldsymbol{x}) = 0 \end{matrix} \tag{18}$$

Each optimization process has been performed using the MOGA algorithm available in the Ansys™ Workbench.

6. Optimization results and discussion

Several optimization procedures have been performed, modifying every time the target heat flux at stagnation point and, consequently, the virtual thermal boundary which the trajectory must lie on.

6.1 Target heat flux $\mathbf{600\ kW/m^2}$

In this subparagraph, the objective function is represented by the area between the trajectory and the re-entry corridor floor over the Mach range $M_\infty = 25$ and M_{Cr}. Therefore, the vehicle TPS is considered perfectly insulating and no safety margin has been assumed.
In Figure 10, the optimization results are shown reporting: the optimal guidance-law (a); the resulting feasible trajectory with respect to the allowable re-entry corridor (b); the resulting heat flux as function of time calculated according to Zoby's relationship (c).

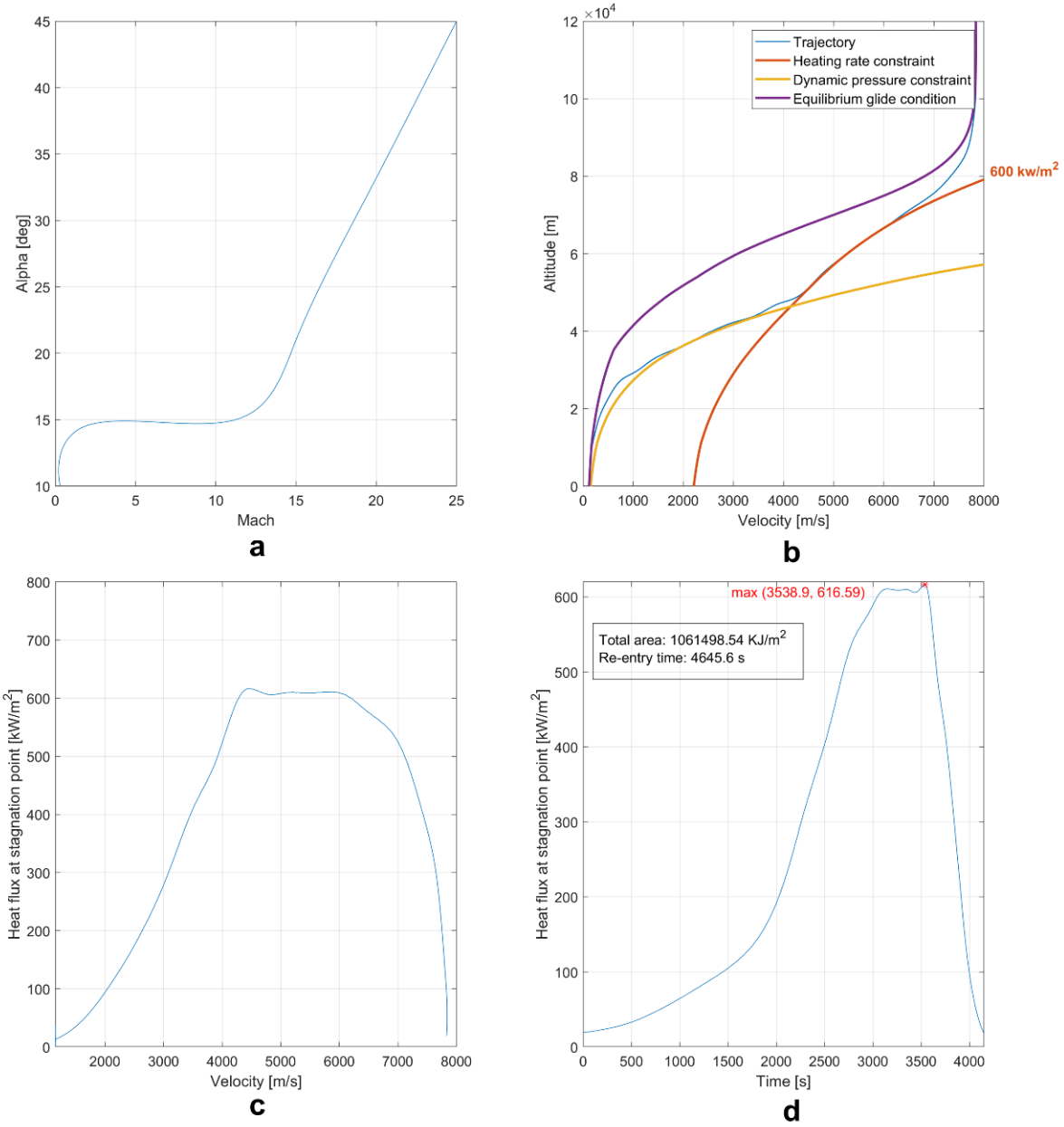

Figure 10 a-d - Optimization results for target heat flux 600 kW/m^2: Guidance law (a); Optimized trajectory (b); Zoby's stagnation point heat-flux vs. velocity (c); Zoby's stagnation point heat-flux vs. time (d).

This procedure considers acceptable a heat flux profile whose peak lies within a 5% range with respect to the prescribed heat flux limit. The heat flux peak value at stagnation point $\dot{q}_{0_{max}}$ is about $617\ \mathrm{kW/m^2}$ and the re-entry time is about 77 minutes, much more that the Space Shuttle, which re-entered in about 30 minutes, with a heat flux peak value of about $700\ \mathrm{kw/m^2}$.
The optimal design vector $\boldsymbol{Y}_{opt}$ is:

$$[\gamma_0, \mu_{a\,0}, Y_1, Y_2, Y_3, Y_4, X_1, X_2, X_3, X_4] = [-0.100, 0.002, 0.886, 0.451, 0.506, 0.627, 0.130, 0.745, 0.769, 0.775] \quad (19)$$

The re-entry trajectory lies inside the feasible region of re-entry corridor (see Figure 10-b) with objective function $\Delta A(\boldsymbol{x}) = 0.6949\ e + 04$. This result is basically due to the ballistic trajectory that occurs at the first period of the re-entry. The only way through which the optimization procedure can reduce the subtended area between the trajectory curve and the thermal constraint curve at higher altitudes is to enter the atmosphere with a nearly positive flight path angle γ_0, causing a skip re-entry.

This circumstance also implies that the material of TPS is not stressed uniformly, generating a variable heat flow at stagnation point, which is dissimilar to the researched aims of this paper.
The optimized guidance law in Figure 10-a shows that the first re-entry phase ($M_\infty > 21$) are performed at $\alpha > 35°$. The heat targeting phase starts at about 6500 m/s where trajectory intersects the thermal boundary. At lower speeds up to about 4500 m/s, trajectory curve superposes to heat flux boundary (Figure 10-b) and the stagnation point heat flux assumes a nearly constant trend (Figure 10-c).

6.2 Target heat flux $\mathbf{575\ kW/m^2}$

For this optimization procedure, the heat flux target $\dot{q}_{0_t}$ has been decreased from $600\ \mathrm{kW/m^2}$ to $575\ \mathrm{kW/m^2}$ keeping the same corridor re-entry boundaries. Also in this case, the procedure was able to find a trajectory that lies on the virtual heating constraint (see Figure 11-b). Therefore, the heat flow trend at stagnation point is nearly constant (see Figure 11-c), and the heat flux peak value at stagnation point $\dot{q}_{0_{max}}$ is lower than that found with the procedure described in the precedent subparagraph ($\sim 598\ \mathrm{kW/m^2}$, see Figure 11-d).

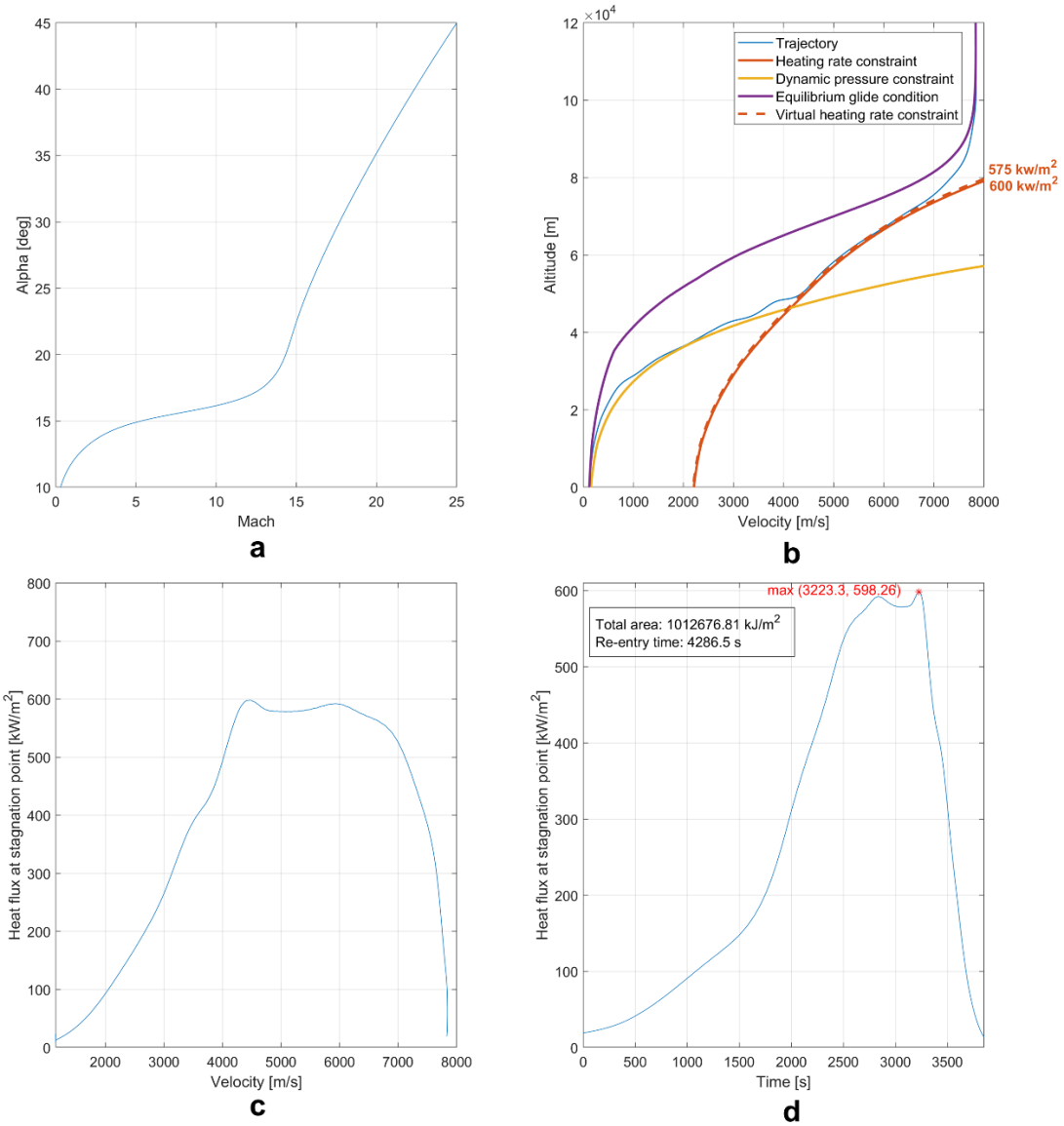

Figure 11 a-d - Optimization results for target heat flux 575 kW/m^2: Guidance law (a); Optimized trajectory (b); Zoby's stagnation point heat-flux vs. velocity (c); Zoby's stagnation point heat-flux vs. time (d).

The re-entry time is about 71 minutes. The optimal design vector $\boldsymbol{Y}_{opt}$ is:

$$[\gamma_0, \mu_{a_0}, Y_1, Y_2, Y_3, Y_4, X_1, X_2, X_3, X_4] = \\ [-0.141, -9.343, 0.612, 0.587, 0.556, 0.629, 0.283, 0.832, 0.802, 0.739] \quad (20)$$

The re-entry trajectory lies inside the feasible region of re-entry corridor (see Figure 11-b) with objective function equal to $\Delta A(\boldsymbol{x}) = 0.6235e + 04$.
The trend of the GL (Figure 11-a) is similar to that found in the precedent subparagraph (Figure 10-a). The trajectory is enforced to lie on a curve (the virtual thermal constraint) that is nearly the same of the heating rate constraint but shifted higher, so the trend of the GL is similar. The major difference is in the curve knee that in this case occurs in at higher AoA. As the trajectory is enforced to reach a lower heat flux peak value, higher AoAs are kept at the same Mach numbers.

6.3 Target heat flux $\mathbf{550\ kW/m^2}$

For this test-case, the heat flux target $\dot{q}_{0_t}$ has been decreased to $550\ \mathrm{kW/m^2}$. The procedure was able to find a trajectory that lies on the virtual heating constraint (see Figure 12-b).

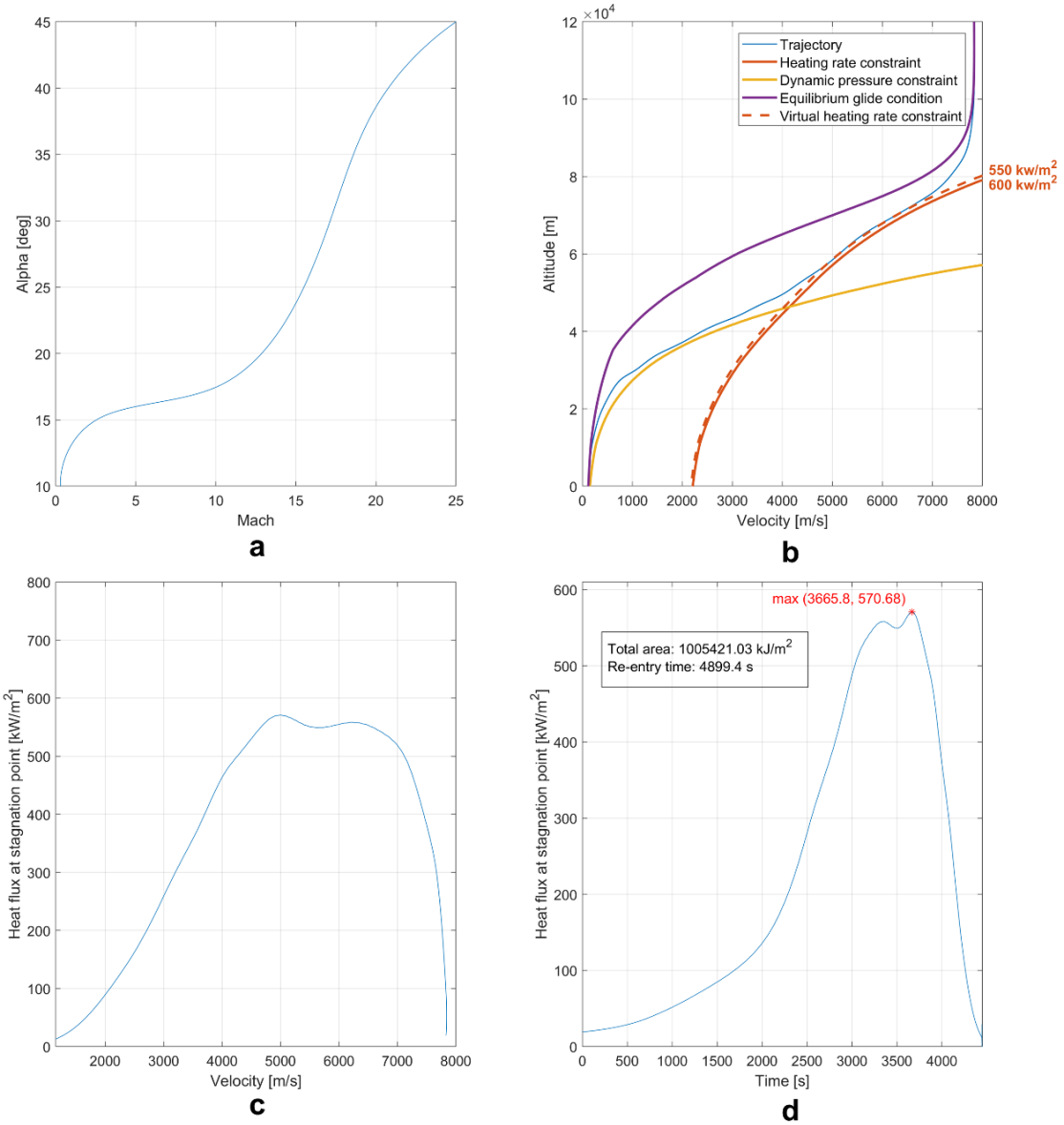

Figure 12 a-d - Optimization results for target heat flux 550 kW/m^2: Guidance law (a); Optimized trajectory (b); Zoby's stagnation point heat-flux vs. velocity (c); Zoby's stagnation point heat-flux vs. time (d).

Therefore, the heat flow trend at stagnation point is nearly constant (see Figure 12-c), and the heat flux peak value at stagnation point $\dot{q}_{0_{max}}$ is lower than that found with the procedures described in

the precedent subparagraphs (~571 $\mathrm{kW/m^2}$, see Figure 12-d).
The re-entry time is about 82 minutes. The optimal design vector $\boldsymbol{Y}_{opt}$ is:

$$[\gamma_0, \mu_{a_0}, Y_1, Y_2, Y_3, Y_4, X_1, X_2, X_3, X_4] = \\ [-0.073, -3.946, 0.663, 0.438, 0.625, 0.801, 0.234, 0.627, 0.827, 0.788] \quad (21)$$

The re-entry trajectory lies inside the feasible region of re-entry corridor (see Figure 12-b) with objective function equal to $\Delta A(\boldsymbol{x}) = 0.6213e + 04$.
Even in this case, the trend of the GL (Figure 12-a) is similar to the previous ones, but for every Mach number the GL curve passes through a higher AoA value to further reduce the heat flow peak.

6.4 Target heat flux $\mathbf{525\ kW/m^2}$

The procedure was able to find a trajectory that lies on the virtual heating constraint $525\ \mathrm{kW/m^2}$ (see Figure 13-b) and this implies that the heat flow trend at stagnation point is nearly constant (see Figure 13-c), with the heat flux peak value at stagnation point $\dot{q}_{0_{max}}$ equal to $\sim 550\ \mathrm{kW/m^2}$ (see Figure 13-d).

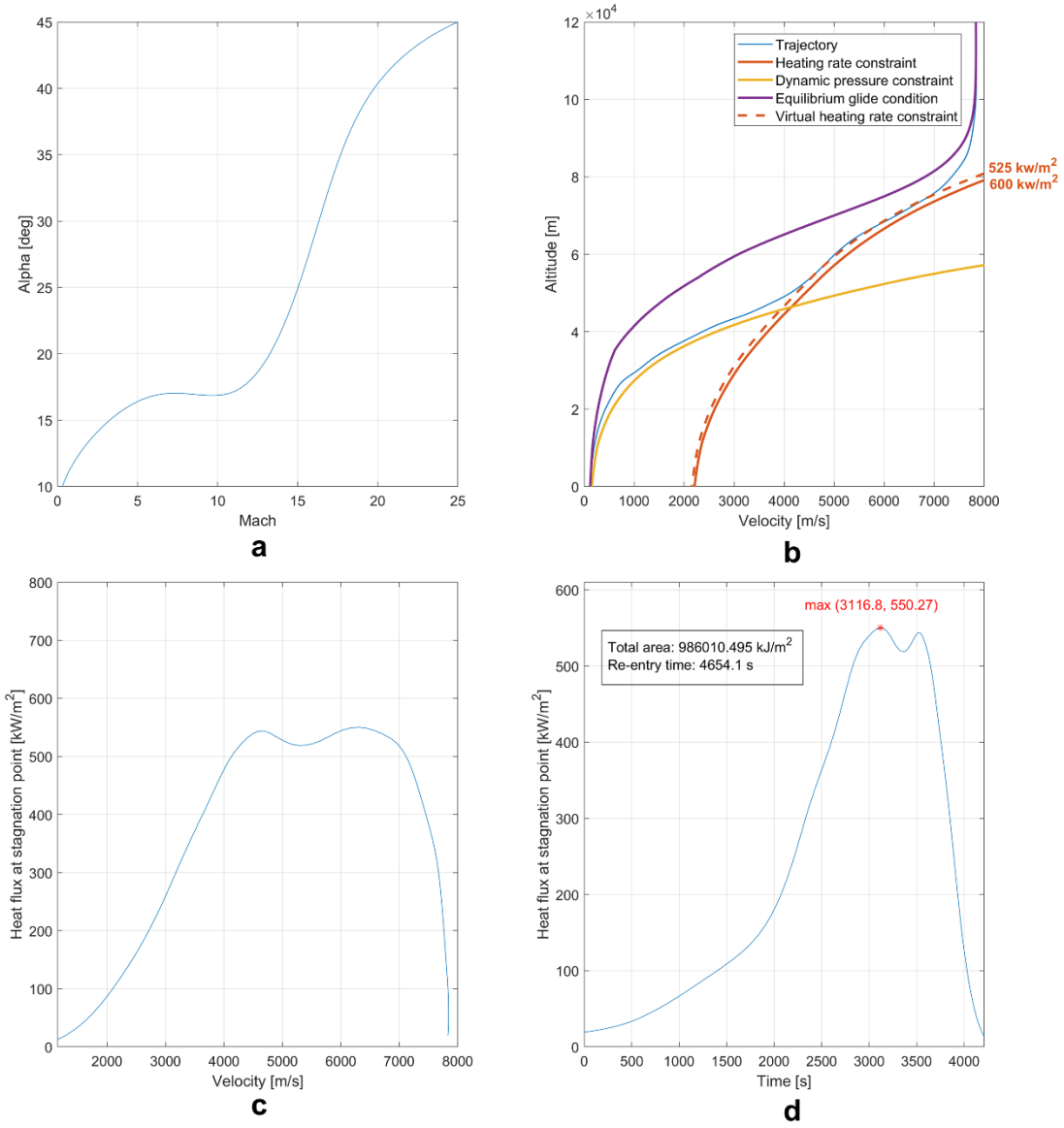

Figure 13 a-d - Optimization results for target heat flux 525 kW/m^2: Guidance law (a); Optimized trajectory (b); Zoby's stagnation point heat-flux vs. velocity (c); Zoby's stagnation point heat-flux vs. time (d).

This value is near to the 5% of the heat flux target because the trajectory curve is slightly below the

thermal constraint. This happens because for the chosen configuration of the vehicle, the optimization procedure cannot find a GL which returns a trajectory capable to give a lower heat flux peak value. In other words, to obtain heat flux peak value lower than $525\ \mathrm{kW/m^2}$ and, at the same time, a heat flow at the stagnation point trend constant, it is necessary to slightly modify the vehicle configuration. The re-entry time is about 78 minutes. The optimal design vector $\boldsymbol{Y}_{opt}$ is:

$$\left[\gamma_0, \mu_{a_0}, Y_1, Y_2, Y_3, Y_4, X_1, X_2, X_3, X_4\right] = [-0.102, 1.659, 0.965, 0.407, 0.592, 0.845, 0.542, 0.694, 0.801, 0.778] \quad (22)$$

The re-entry trajectory lies inside the feasible region of re-entry corridor (see Figure 13-b) with objective function equal to $\Delta A(\boldsymbol{x}) = 0.6407e + 04$.
Even in this case, the trend of the GL (Figure 13-a) is similar to the trends found in the precedent subparagraphs, but for every Mach number the GL curve passes through a higher AoA value to further reduce the heat flow peak.

6.5 Target heat flux $\mathbf{500\ kW/m^2}$

The procedure leads to the trajectory shown in Figure 14-b, with the heat flux peak value at stagnation point $\dot{q}_{0_{max}}$ equal to $\sim 536\ \mathrm{kW/m^2}$ (see Figure 14-d).

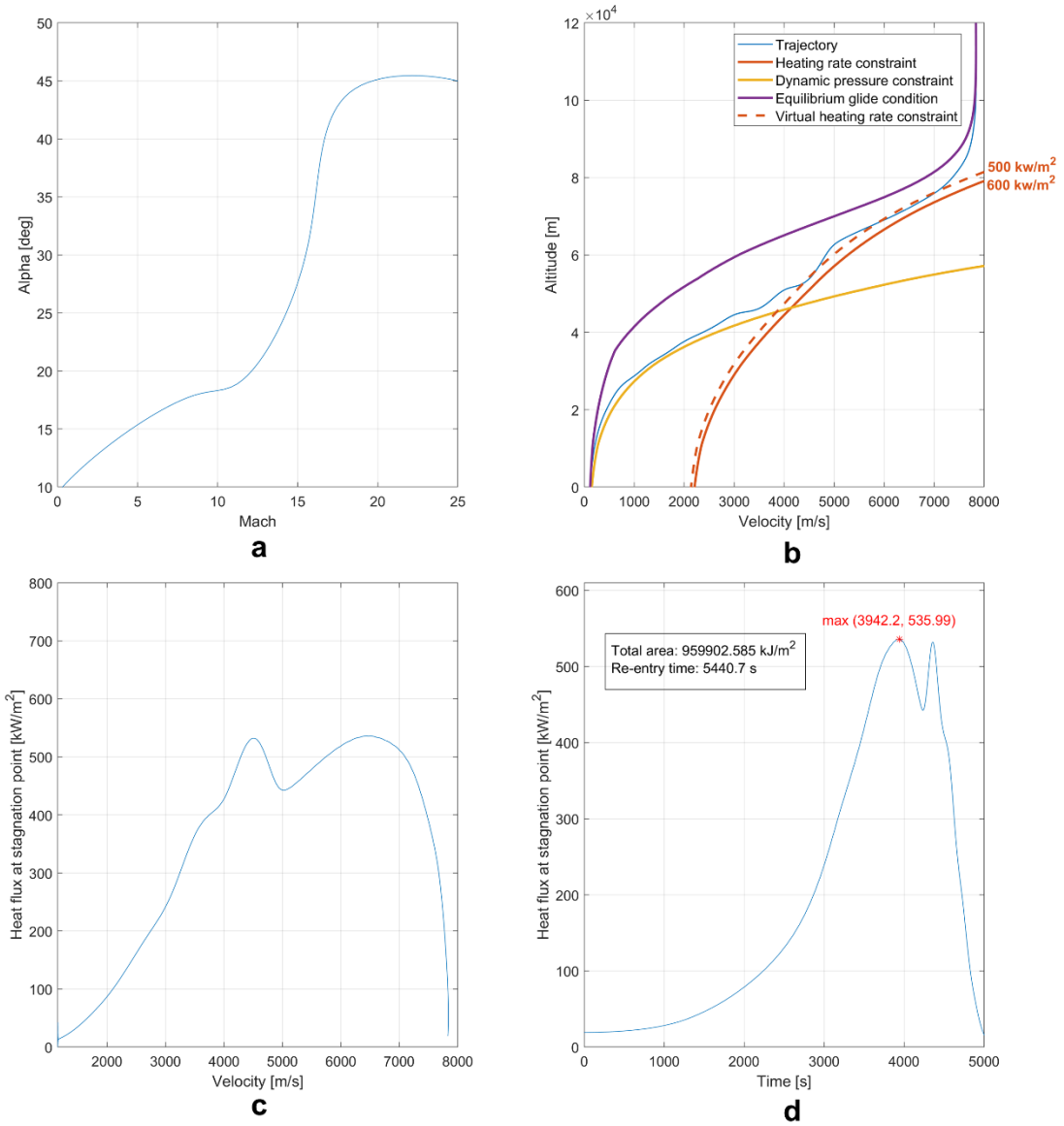

Figure 14 a-d - Optimization results for target heat flux 500 kW/m^2: Guidance law (a); Optimized trajectory (b); Zoby's stagnation point heat-flux vs. velocity (c); Zoby's stagnation point heat-flux vs. time (d).

In this case, the heat flux peak value is slightly greater than the 5% of the heat flux target, as expected from the previous test-case. As shown in Figure 14-b, the trajectory does not lie on the thermal boundary and, consequently, the heat flux trend at the stagnation point is not so constant, presenting two non-negligible peaks.
The re-entry time is about 91 minutes. The optimal design vector $\boldsymbol{Y}_{opt}$ is:

$$[\gamma_0, \mu_{a_0}, Y_1, Y_2, Y_3, Y_4, X_1, X_2, X_3, X_4] = [-0.002, 1.568, 0.899, 0.425, 0.607, 0.976, 0.763, 0.708, 0.846, 0.733] \quad (23)$$

The re-entry trajectory lies inside the feasible region of re-entry corridor (see Figure 14-b) with objective function equal to $\Delta A(\boldsymbol{x}) = 0.8838e + 04$. It is important to notice that this value is bigger than those obtained in the precedent subparagraphs because the trajectory curve does not lie on the thermal constraint curve.

6.6 Comparison

In Table 1, some relevant features can be observed for each heat flux level.

Table 1 - General features.

	$\dot{q}_{0_t}$ [kW/m²]				
	600	**575**	**550**	**525**	**500**
$\dot{q}_{0_{max}}$ [kW/m²]	617	598	571	550	536
$A_{\dot{q}_0}$ [MJ/m²]	1061	1013	1005	986	960
Δt [s]	4646	4285	4899	4654	5441
γ_0 [deg]	-0.100	-0.141	-0.073	-0.102	-0.002
μ_{a_0} [deg]	0.002	-9.343	-3.946	1.659	1.568
Δx_p [m]	27487	25029	29637	27937	34208
Δy_p [m]	11	-653	-287	119	105

The heat flux peak value $\dot{q}_{0_{max}}$ increases as the heat flux target $\dot{q}_{0_t}$ with an almost linear trend (Table 1 and Figure 15). Therefore, the lowest heat flux peak ($536\ \mathrm{kW/m^2}$) occurs in the case of heat flux target $500\ \mathrm{kW/m^2}$, while the upper heat flux peak ($617\ \mathrm{kW/m^2}$) occurs in the case of heat flux target coincident with the floor of the re-entry corridor ($600\ \mathrm{kW/m^2}$).

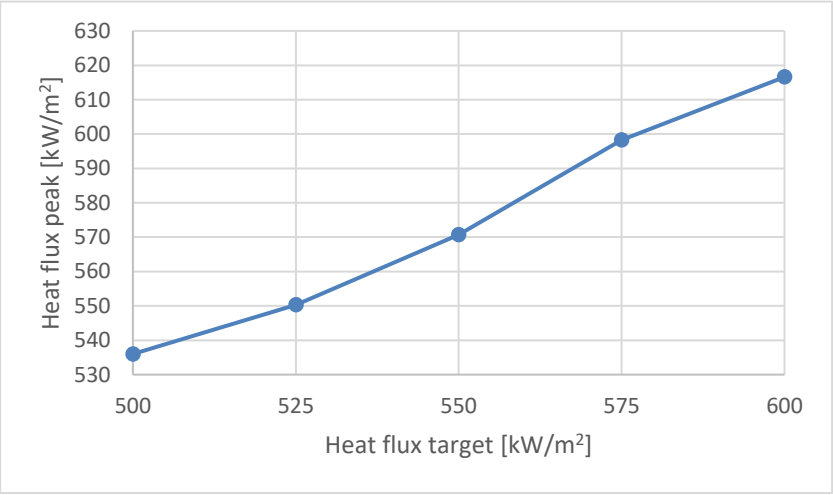

Figure 15 - Heat flux peak trend.

The heat flux total area $A_{\dot{q}_0}$ increases with the heat flux target $\dot{q}_{0_t}$ (Table 1 and Figure 16). It means that the lower is the heat flux target, the lower is the total energy amount stored inside the TPS;

therefore, by reducing the heat flux target, it is possible to use a thinner TPS, with consequent reduced costs.

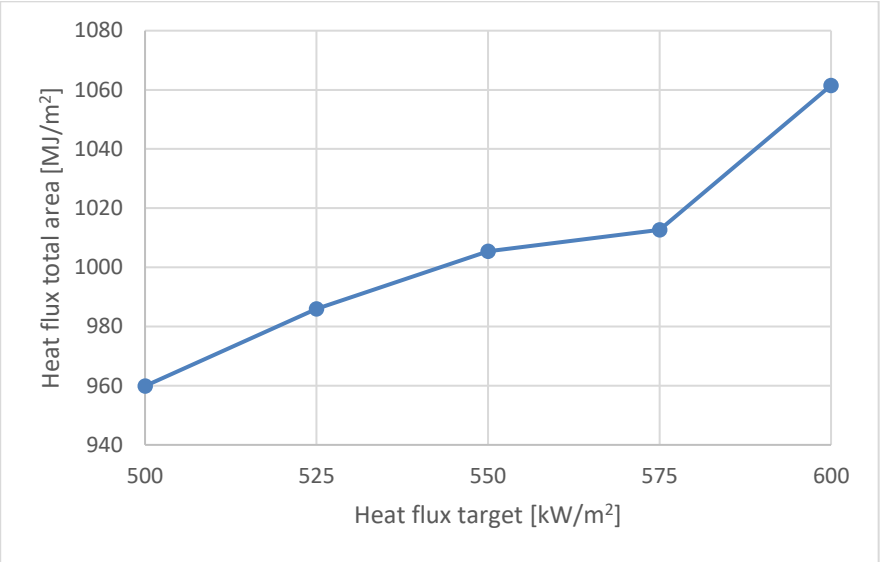

Figure 16 - Heat flux total area trend.

The re-entry time values are the result of the flight path angle chosen by the optimization procedure. For example, from Table 1 it is possible to notice that the optimization procedure has given a re-entry time of about 91 minutes for the case of heat flux target $500\ \mathrm{kW/m^2}$ and a re-entry time of about 71 minutes for the case of heat flux target $575\ \mathrm{kW/m^2}$.
The flight path angle γ_0 chosen by the optimization procedure for the case of heat flux target of $500\ \mathrm{kW/m^2}$ is less than the homologous one chosen for the heat flux target of $575\ \mathrm{kW/m^2}$ (-0.002° vs. -1.141°, as shown in Table 1). This happens because the higher is the heat flux target, the narrower is the virtual re-entry corridor (the re-entry corridor which has the virtual thermal constraint as floor), and the shorter is the ballistic phase.
Consequently, the optimization procedure choses a higher flight path angle to allow the trajectory to lie on the virtual thermal constraint (see Eq. (9)).
As described in Eq. (10), the re-entry time is also affected by the bank angle. Therefore, as shown in Table 1, the lower heat flux target corresponding to the higher re-entry time, is characterized by the lower (in modulus) γ_0 and one of the lowers (in modulus) μ_{a_0}.

7. Conclusions

In the present paper, a preliminary feasibility study for a new re-entry strategy for future manned missions performed by a high S_r/m vehicle, has been presented. A re-entry approach based on a gradual dissipation of total energy has been assumed by increasing the re-entry flight time and performing a shallower re-entry able to guarantee a safer re-entry mission. Different heat flux levels have been analyzed to ensure a constant trend for the heat flux at stagnation point, which makes possible to employ a re-usable TPS, with a safety margin as higher as possible with respect to the floor of the re-entry corridor. For a heat flux level of $500\ \mathrm{kW/m^2}$, about a 10% safety margin is guaranteed, but the heat flux trend at stagnation point is not constant.
For a heat flux level of $525\ \mathrm{kW/m^2}$, the safety margin is about 8.5% with a heat flux trend at stagnation point almost constant. For higher heat flux levels, the heat flux trend at stagnation point is constant but the safety margin tends towards zero. To further decrease the flux level, it is necessary starting from a different vehicle shape design. For every heat flux level analyzed, the re-entry time is much greater than the Space Shuttle one (from about 71 minutes to about 91 minutes). This means that the spacecraft performs a shallower re-entry and this helps to keep lower peak flux levels.

8. Contact Author Email Address

Author e-mail address for future contacts is: nicolina.montella@unicampania.it

9. Copyright Statement

References

[1] Q. Han, C. Sun, Y. Tao, Z. Li, Y. Zhang and Y. Chen, "Thermal protection of a hypersonic vehicle by modulating stagnation-point heat flux," *Aerospace Science and Technology,* vol. 98, 2020.

[2] A. Aprovitola, L. Iuspa, G.Pezzella, and A. Viviani, Phase A design of a reusable re-entry vehicle, ACTA Astronautica, 2021.

[3] A. Cusick and K. Kontis, "Creation of design and analysis tools for Large Design Space reusable launch vehicle shape optimization," in *AIAA Aviation 2019 Forum*, Dallas, TX, 2019.

[4] A. Viviani, L. Iuspa and A. Aprovitola, "An optimization-based procedure for self-generation of re-entry vehicles shape," *Aerospace Science and Technology,* vol. 68, pp. 123-134, 2017.

[5] A. Viviani, L. Iuspa and A. Aprovitola, "Multi-objective optimization for re-entry spacecraft conceptual design using a free-form shape generator," *Aerospace Science and Technology,* vol. 71, pp. 312-324, 2017.

[6] A. Aprovitola, L. Iuspa and A. Viviani, "Thermal protection system design of a reusable launch vehicle using integral soft objects," *International Journal of Aerospace Engineering,* vol. 105, 2019.

[7] A. Viviani, A. Aprovitola, L. Iuspa and G. Pezzella, "Aeroshape design of reusable re-entry vehicles by multidisciplinary optimization and computational fluid dynamics," *Aerospace Science and Technology,* vol. 105, 2020.

[8] U. Walter, Astronautics, The Physics of Space Flights, Switzerland: Springer International Publishing, 2018.

[9] A. Aprovitola, N. Montella, L. Iuspa, G. Pezzella and A. Viviani, "An optima heat-flux targeting procedure for LEO re-entry of resuable vehicles," *Aerospace Science and Technology,* vol. 112, 2021.

[10] H. Zhou, X. Wang and N. Cui, "Glide guidance for reusable launch vehicles using analytical dynamics," *Aerospace Science and Technology,* vol. 98, 2020.

[11] M. W. Guo and D. Y. Wang, "Guidance law for low-lift skip reentry subject to control saturation based on nonlineare predective control," *Aerospace Science and Technology,* vol. 43, 2015.

[12] B. Tian and Q. Zong, "Optimaf guidance for reentry vehicles based on indirect Legendre pseudospectral method," *Acta Astronautica,* vol. 68, 2011.

[13] E. Mooij, "Heat-flux tracking for thermal protection system testing," in *AIAA/AAS Astrodynamics Specialist Conference,* San Diego, California, 2017.

[14] P. Vernis, V. Morio and E. Ferreira, "Genetic algorithm for coupled rlv trajectory and guidance optimization," *IFAC Proceedings Volumes,* vol. 40, no. 7, 2007.

[15] C. Chawla, P. Sarmah and R. Padhi, "Suboptimal reentry guidance of a reusable launch vehicle using pitch plane maneuever," *Aerospace Science and Technology,* vol. 14, no. 6, pp. 377-386, 2010.

[16] D.-J. Zhao and Z.-Y. Song, "Reentry trajectory optimization with waypoint and no-fly zone constraints using multiphase convex programming," *Acta Astronautica,* vol. 137, pp. 60-69, 2017.

[17] A. Viviani, A. Aprovitola, L. Iuspa and G. Pezzella, "Low speed longitudinal aerodynamics of a blended wing-body re-entry vehicle," *Aerospace Science and Technology,* vol. 107, 2020.

[18] D. Stanley, "Space trasportation architecture for the future," *Acta Astronautica,* vol. 47, no. 2-9, pp. 265-274, 2000.

[19] A. Aprovitola, N. Montella, L. Iuspa, G. Pezzella and A. Viviani, "Aerodynamic and Aerothermaldynamic Assestment of a Lifting-Body Re-Entry Vehicle," in *33rd Congress of the International Council of the Aeronautical Science,* Stockholm, 2022.

[20] H. Schlichting and K. Gersten, Boundary-Layer Theory, Berlin, Heidelberg: Springer, 2017.

[21] E. H. Hirschel and C. Weiland, Selected Aerothermodynamic Design Problems of Hypersonic Flight Vehicles, Springer, 2009.

[22] O. Uyanna and H. Najafi, "Thermal protection system for space vehicles: a review on technology developement, current challenges and future prospects," *Acta Astronautica,* vol. 176, pp. 341-356, 2020.